Dehalogenation and Coupling of Polycyclic Hydrocarbon on an Atomically Thin Insulator

Journal:	*ACS Nano*
Manuscript ID:	nn-2014-01906w.R1
Manuscript Type:	Article
Date Submitted by the Author:	05-Jun-2014
Complete List of Authors:	Dienel, Thomas; EMPA, nanotech@surfaces Laboratory Goméz-Díaz, Jaime; University of Zurich, Institute of Physical Chemistry Seitsonen, Ari; University of Zurich, Institute of Physical Chemistry Widmer, Roland; EMPA, nanotech@surfaces Laboratory Iannuzzi, Marcella; University of Zurich, Institute of Physical Chemistry Radican, Kevin; EMPA, nanotech@surfaces Laboratory Sachdev, Hermann; Max-Planck-Institute for Polymer Research, Müllen, Klaus; Max-Planck-Institute for Polymer Research, Hutter, Juerg; University of Zurich, Institute of Physical Chemistry Groening, Oliver; Empa, nanotech@surfaces Laboratory

SCHOLARONE™
Manuscripts

Dehalogenation and Coupling of a Polycyclic Hydrocarbon on an Atomically Thin Insulator

Thomas Dienel[1]*, Jaime Gómez-Díaz [†2], Ari P Seitsonen[2], Roland Widmer[1], Marcella Iannuzzi[2],

Kevin Radican[1], Hermann Sachdev[3], Klaus Müllen[3], Jürg Hutter[2], and Oliver Gröning[1]*

* Thomas Dienel: thomas.dienel@empa.ch

* Oliver Gröning: oliver.groening@empa.ch

[1]   Empa - Swiss Federal Laboratories for Materials Science and Technology,

         nanotech@surfaces Laboratory, CH-8600 Dübendorf, Switzerland.

[2]   University of Zurich, Department of Chemistry, Winterthurerstrasse 190,

         CH-8057 Zurich, Switzerland.

[3]   Max Planck Institute for Polymer Research, Department of Synthetic Chemistry,

         Ackermannweg 10, D-55128 Mainz, Germany.

Catalytic activity is of pivotal relevance in enabling efficient and selective synthesis processes. Recently, covalent coupling reactions catalyzed by solid metal surfaces opened the rapidly evolving field of on-surface chemical synthesis. Tailored molecular precursors in conjunction with the catalytic activity of the metal substrate allow the synthesis of novel, technologically highly relevant materials such as atomically precise graphene nanoribbons. However, the reaction path on the metal substrate remains unclear in most cases and the intriguing question is how a specific atomic configuration between reactant and catalyst controls the reaction processes. In this study, we cover the metal substrate with a monolayer of hexagonal boron nitride (*h*-BN), reducing the reactivity of the metal, and gain unique access to atomistic details during the activation of a polyphenylene precursor by sequential dehalogenation and the subsequent coupling to extended oligomers. We use scanning tunneling microscopy (STM) and density functional theory (DFT) to reveal a reaction site anisotropy, induced by the registry mismatch between the precursor and the nano-structured h-BN monolayer.

KEYWORDS

on-surface reaction, scanning tunneling microscopy, PAH, porous graphene, hexagonal boron nitride, boronitrene, nanomesh

An atomically thin layer of insulating *h*-BN is a structurally analogous counterpart for graphene – a single layer of sp^2-hybridised carbon atoms[1] – matching the graphene lattice almost perfectly with a small mismatch of approx. 2%. Currently, the fabrication of two-dimensional materials follows two main approaches: *i*) the bottom-up synthesis by substrate supported chemical vapor deposition (CVD) with suitable precursors and *ii*) the top-down approach by exfoliation. The assembly of graphene/*h*-BN heterostructures, leading to novel devices or devices with enhanced performance, usually relies on elaborate, sequential transfer processes of the produced layers.[2] The main obstacles are possible misalignment, introduction of defects and contaminations resulting from transferring layers that are just one atom thick. Only recently, the direct CVD growth of graphene on *h*-BN was demonstrated, offering superior properties.[3-5] However, the growth conditions are harsh (long exposure time, high temperatures, several cycles, etc.). Metal substrates are favored, because of their high catalytic activity,[6] but they have the disadvantage that they strongly alter the properties of the grown layers, which therefore cannot be directly used for electronic device fabrication.

A common motif in on-surface chemical reactions is the activation of a precursor, the intermittent complex formed between precursor and substrate, and finally the coupling reaction.[7] A long-standing question is the impact of the specific atomic configuration between substrate and reactant on the catalytic efficiency and how does the specific atomic arrangement change the site activity and therefore influence the reaction pathways, energies and reaction yield? Thanks to recent advances in surface science, we are witness of a tremendous progress in the understanding and development of on-surface chemical reactions and in the fabrication of nanostructured systems.[7-9] A widely used reaction in this context is derived from Ullmann coupling,[10,11] where the reactive partners are created by dehalogenation of aryl-halide precursors,

which subsequently undergo aryl-aryl coupling.[12] Recent examples of this are the formation of graphene nanoribbons and porous graphene on metal substrates.[13-15] The synthesis of porous graphene is based on the molecular precursor 5,5′,5″,5‴,5⁗,5⁗′-hexaiodo-cyclohexa-m-phenylene (I_6-CHP, *cf.* inset in Fig. 1a for chemical structure), which dissociates all its iodine atoms on Cu(111), Ag(111) and even Au(111) already at room temperature.[15] The catalytic activity is so high that site specific effects are difficult to study and do not seem relevant for the synthesis process. This situation can be expected to be different for a surface supported, ultra-thin insulating spacer layer like monolayer *h*-BN, in analogy to graphene sometimes referred to as boronitrene.[16] The lack of electronic states close to the Fermi level will reduce the catalytic activity, whereas the ultimate thinness still allows the dehalogenation process to be studied by STM. Furthermore, the interaction between the metal and *h*-BN layer generates distinct superstructures that can be adjusted by a variation of the underlying metal (Ni,[17] Pt,[18] Cu,[19] Rh and Ru,[18,20-26] Fe and Cr[27,28]). On Rh(111) the *h*-BN forms a highly corrugated "nanomesh" consisting of regions with strong bonding, dents (sometimes referred to as pores), separated by suspended wire regions, where the *h*-BN-Rh(111) interaction is weaker.[18,23,26,29-31] Consequently, the structure of the corrugated *h*-BN is a superposition of the 0.25 nm BN lattice and the network of dents with a lattice constant of 3.2 nm.

As we will show in the following, deposition of I_6-CHP on the corrugated *h*-BN leads to a distinct adsorption geometry imposing a non-equivalency on the six iodine sites of the molecule, which is not intrinsic to the free I_6-CHP. The adsorption geometry, sequential dehalogenation and the subsequent coupling of I_x-CHP species are analyzed by low-temperature scanning tunneling microscopy (LT-STM at 5.5 K) and density functional theory (DFT). Our experimental and theoretical findings show that the dehalogenation process is surprisingly strongly influenced

by the substrate and they shed light on the challenges of growing bottom-up designed nanostructures directly on an insulating substrate, being indispensable for efficient application in electronic, optic and spintronic devices.

Results and discussion

The nanoscale petri dish for molecules. Figure 1a displays an UHV LT-STM image with low coverage (approx. 0.15 ML) of I_6-CHP deposited onto the corrugated h-BN (kept at RT during deposition). Empty dents are imaged as dark depressions.[18,23] while the adsorbed molecules exhibit a six petal flowerlike appearance originating from the apparent D_6 symmetric structure of a single I_6-CHP. All molecules occupy single dents and are well-separated from each other and follow the same registry as the superstructure of the corrugated h-BN. This situation is entirely different compared to molecules on other insulating thin films typically used in STM – like alkali metal salts (NaCl, KCl, etc.) on metals. The rather homogenous structure of these dielectric spacers is of manifold advantage to studying individual molecules.[32-34] However, the adsorption energy landscape for molecular species usually shows only subtle corrugation and already at low coverage (well below a closed monolayer) immediate 2-dimensional domain formation is observed, with molecular close-packing or even aggregation into 3-dimensional structures similar to single crystal insulators.[35,36]
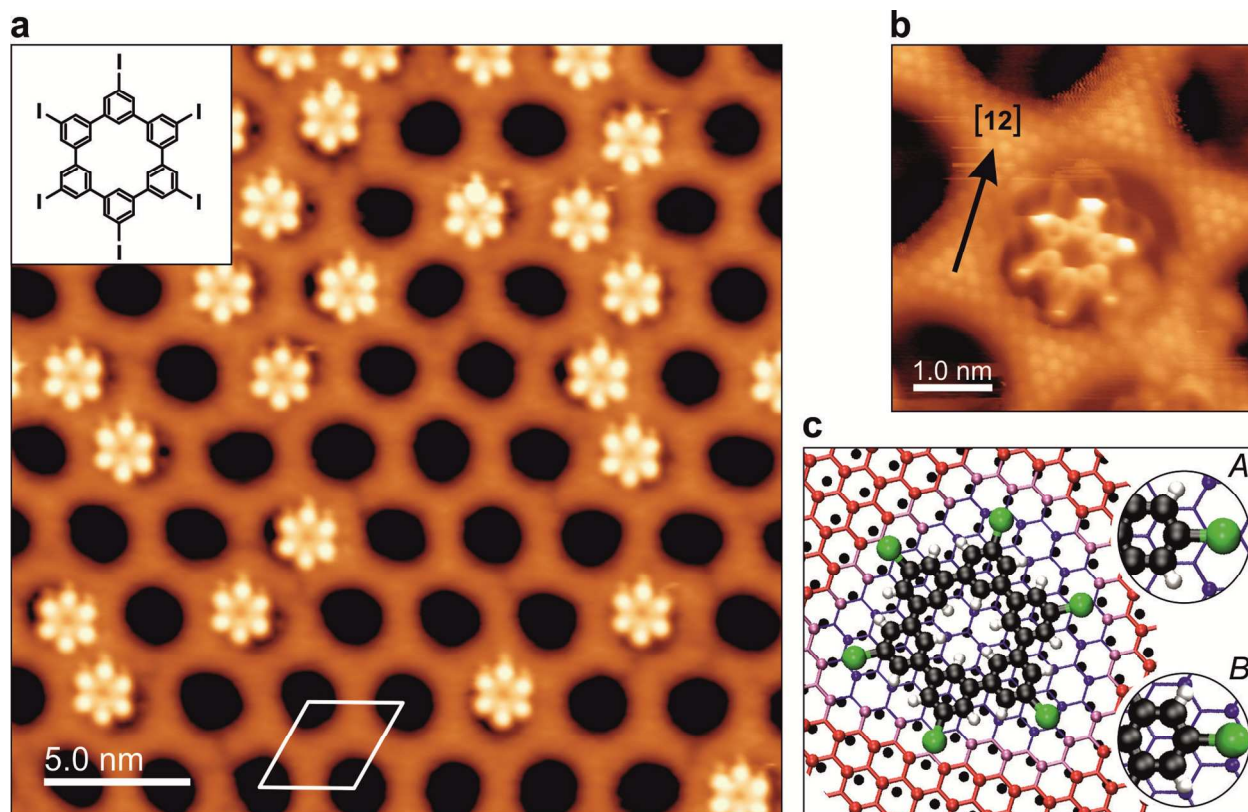
Figure 1: Molecule I$_6$-CHP and the corrugated *h*-BN. a, STM image (-1.70 V, 40 pA) of I$_6$-CHP molecules occupying some of the dents of the corrugated *h*-BN (low coverage of 0.15 ML, height scale: $\Delta z = 170$ pm, inset: molecular structure). **b**, High resolution STM image (-1.2 V, 32 pA, (height scale: $\Delta z = 170$ pm)) of a single molecule, revealing internal contrast of the *h*-BN layer and submolecular contrast of the molecule. **c**, Ball and stick model of the DFT derived position and orientation of the I$_6$-CHP in the dents of the corrugation (boron atoms of *h*-BN lattice enlarged; dent indicated by color coding; black dots indicate top layer of rhodium atoms). The two insets show the different registries for the carbon-iodine bond: hollow position = *A* site; on top boron = *B* site (rhodium atoms are omitted for clarity reasons).

Here on the corrugated *h*-BN, all intermolecular distances are well defined by the superstructure lattice of the dents, which are large compared to those found in close-packed I_6-CHP domains. Therefore, the intermolecular interactions between neighboring molecules are negligible and the species can be treated as isolated molecules, interacting solely with the *h*-BN/metal substrate. Figure 1a shows the regular adsorption geometry of I_6-CHP molecules within the dents. Two major observations can be drawn immediately: *i*) the molecules systematically adsorb close to the rim rather than at the center of a dent (the center-center distance between molecule and dent is 0.48+/-0.09 nm) and *ii*) a clear preferential orientation for I_6-CHP in the dent can be observed. Within the measurement accuracy of 1° all molecules are perfectly oriented along the [12] direction of the *h*-BN corrugation. The preferential orientation is confirmed by the DFT calculations (*cf*. Supplementary Information) and proves the existence of a specific registry of the molecule and the *h*-BN lattice. While the geometry of an I_6-CHP molecule in the gas phase, as optimized by DFT, exhibits D_3 symmetry of alternating up-down tilted phenyl rings, this buckling diminishes on the substrate, which is consistent with STM images, where the molecules appear as planar (*cf*. high resolution STM imaging in Fig. 1b).

The shape and size of the STM image of the molecule (outer diameter approx. 15 Å) clearly indicate that all the six iodine atoms are still covalently bonded to the aromatic macrocycle. This is in strong contrast to the case of I_6-CHP on metals, where the iodine atoms already dissociate at room temperature, leaving a sizeable space between the iodine atoms and the molecular remnant.[14,15] The non-dissociated I_6-CHP molecules on the *h*-BN confirm the reduced catalytic activity of BN already at the monolayer thickness on a metallic substrate. Detailed analysis of the atomic contrast of *h*-BN and the I_6-CHP position in the high resolution STM images and DFT calculations suggest that the molecules are centered above the nitrogen atoms (*cf*. Fig. 1c), with

the I_6-CHP's carbon atoms on-top of boron or on hollow sites of the h-BN. This yields to two alternating, non-equivalent sites of the C-I groups with respect to the h-BN substrate, reducing the apparent 6-fold symmetry of the I_6-CHP to an effective 3-fold one. As shown in Fig. 1c, the site denoted by A is characterized by the carbon atom of the C-I group located on top of a h-BN hollow site. For the B site, the carbon atom is located on top of a boron atom.

Tip-induced dehalogenation of a single molecule

The fact that the I_6-CHP stays intact when deposited onto the corrugated h-BN layer offers a unique opportunity to study the dissociation of its iodine atoms individually and in detail. Under some tunneling conditions, we observed a low yield, spontaneous STM tip induced dehalogenation of the I_6-CHP. Figure 2 displays several stages of a typical dehalogenation sequence of a single I_6-CHP molecule, exhibiting three remarkable features: i) the iodine atoms dissociate at alternating positions around the molecule, ii) the dehalogenation comes to a halt after removing three iodine atoms and iii) the dissociated iodine atoms and the molecule can stay in close proximity within one dent. Since in the gas phase the iodine dissociation energy is the same irrespective of the iodine sites and also of the number of already dissociated iodine atoms, the deviations seen here are obviously an effect of the interaction with the substrate, (2 eV from a DFT calculation, $cf.$ Supplementary Information). In other words, the free I_6-CHP molecule does not possess intrinsic site correlation with regard to the dehalogenation process. As a consequence, neither I_3-CHP species (alternating 5′,5‴,5″‴‴-I_3-CHP or continuous 5‴,5″″,5″‴‴-I_3-CHP) should exhibit an accentuated stability.
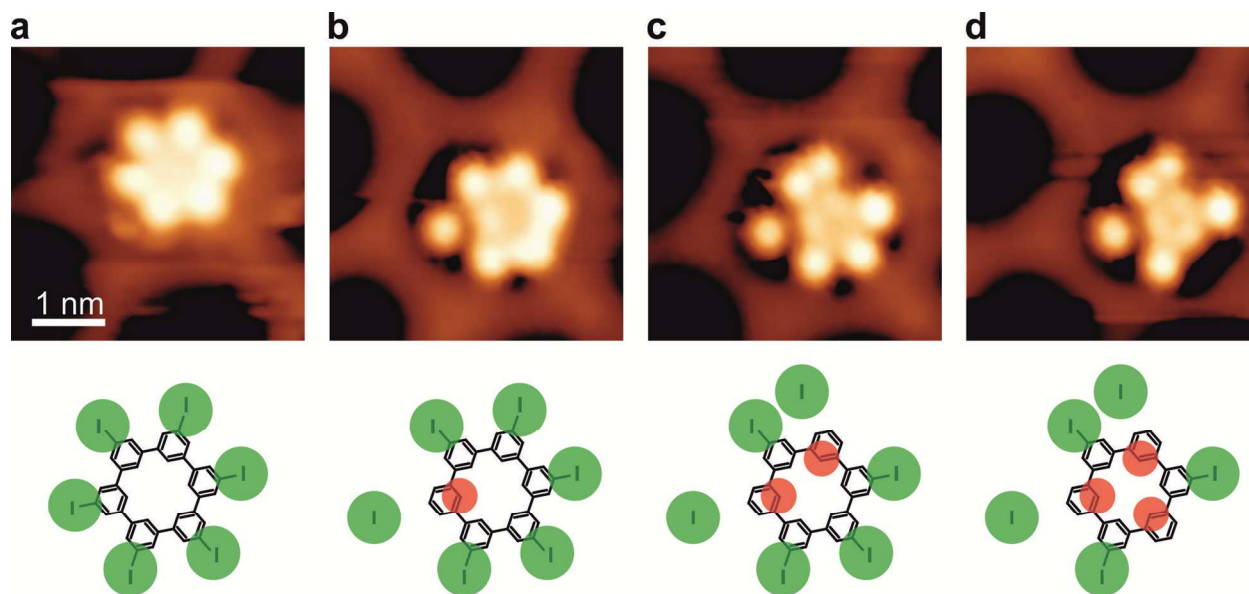
Figure 2: Sequence of STM images during tip-induced iodine dissociation. **a-d**, Close up STM images (top) and illustrative diagrams (bottom) of the sequential dehalogenation (height scale: $\Delta z = 170$ pm). **a**, The six lobes of the intact molecule (1.1 V, 100 pA) are formed by iodine atoms (schematically shown in green). **b-d**, The continuously applied tip-sample current (1.5 V, 100 pA) during on-going STM scans leads to the dissociation of iodine atoms from I_6-CHP at specific positions (*i.e.* the *B* sites: b, at 5′′′′′, c, at 5′, and d, at 5′′′). The actual sequence is random. The highest accessible state of dissociation by this approach is the I_3-CHP (d). The dissociated iodine atoms can stay within the dent without affecting the molecular remnant or be removed by the tip (d). Please note the appearance of small protrusions (schematically drawn in red) close to the center of the molecule after removing the corresponding iodine atom.

On the corrugated *h*-BN instead, the registry between molecule and substrate lifts the equivalency between the different iodine sites. The regularly observed case is that the iodine atoms subsequently dissociate at positions 5′,5′′′, or 5′′′′′ (*cf.* Fig. 2b to d) – which corresponds to the *B* sites of the previously assigned adsorption geometry (*cf.* Fig. 1c). The investigation of

numerous STM tip-induced dehalogenation events shows that the sequence among the three

B sites is random and does not involve detectable movement of the molecule. Additionally, once

the covalent iodine-carbon bond is broken, the separated lobe of the detached iodine atom

appears accompanied by a protrusion on the CHP backbone close to the newly formed radical

position. As this protrusion is visible at STM bias voltages well within the HOMO-LUMO gap,

we attribute it to a change in the conformation of the molecule rather than to an electronic effect.

As we will discuss later on, DFT calculations show that the conformational change is caused by

a bond formation of the radical site with the underlying boron atom. Such a bond locks the

molecule in position and consequently favors the remaining alternating sites – which are now

locked above boron atoms – for dehalogenation, *i.e.*, dissociation at all the B sites.

However, in some rare cases the first iodine atom of I_6-CHP dissociates at an A site. Only then,

the dehalogenation is accompanied by a small but well observable relocation of the molecule (cf.

Supporting Fig. S2). This shift was first revealed by the DFT structure optimization of the

dehalogenated molecule and afterwards recognized in the experiments. Indeed, the shift is

necessary to form the carbon-boron bond, since the carbon atom is initially, *i.e.* before

dehalogenation, on top of a hollow site. In the new position and consequently new registry to the

substrate, the options for further dehalogenation of the molecule are limited and the opposing

iodine atom is predominantly dissociated. The two bonds between molecule and substrate

effectively suppress additional dehalogenations at the remaining iodine sites, *e.g.* a stable

$5',5'',5'''',5'''''$-I_4-CHP results. Summarizing, complete dissociation at B sites – forming $5,5'',5''''$-

I_3-CHP – is by far the most commonly observed dehalogenation state and also marks the limit of

tip-induced dehalogenation during continuous STM imaging. In cases, where we observe

dehalogenation at an A site, it is predominantly followed by the iodine abstraction at the

opposing *B* site. In these cases the tip-induced dehalogenation stops with the formation of I_4-CHP.

Dehalogenation by thermal annealing

In order to further corroborate our findings on the orientation and site selectivity of the iodine abstraction, we conducted thermally activated dehalogenation experiments. Figure 3a shows the LT-STM image after heating the sample to approx. 500 K for 15 min. A large variety of molecular species is visible, differing in the degree of dissociation (number of radical sites) and the specific position where the iodine atoms dissociated from. Unlike in the tip-induced case, here the dissociated iodine usually cannot be found in the dents with the molecule. The atoms generally desorb from the surface or aggregate forming iodine islands. Despite the different stages of dehalogenation nearly all molecular species are oriented along the [12] direction of the *h*-BN corrugation. Counting the created I_x-CHP species over a larger field of view (*cf.* supporting figure S1), more than 95% of all observed dehalogenated positions turn out to be at *B* sites of the molecule-*h*-BN registry. This motif of preferred dehalogenation sites gets even more evident when three iodine atoms dissociate, leading to the three-fold symmetric I_3-CHP with only *B* site dissociations. It nicely confirms the observation made before that the first dissociation at the I_6-CHP molecule constrains the available sites for subsequent dehalogenation steps.
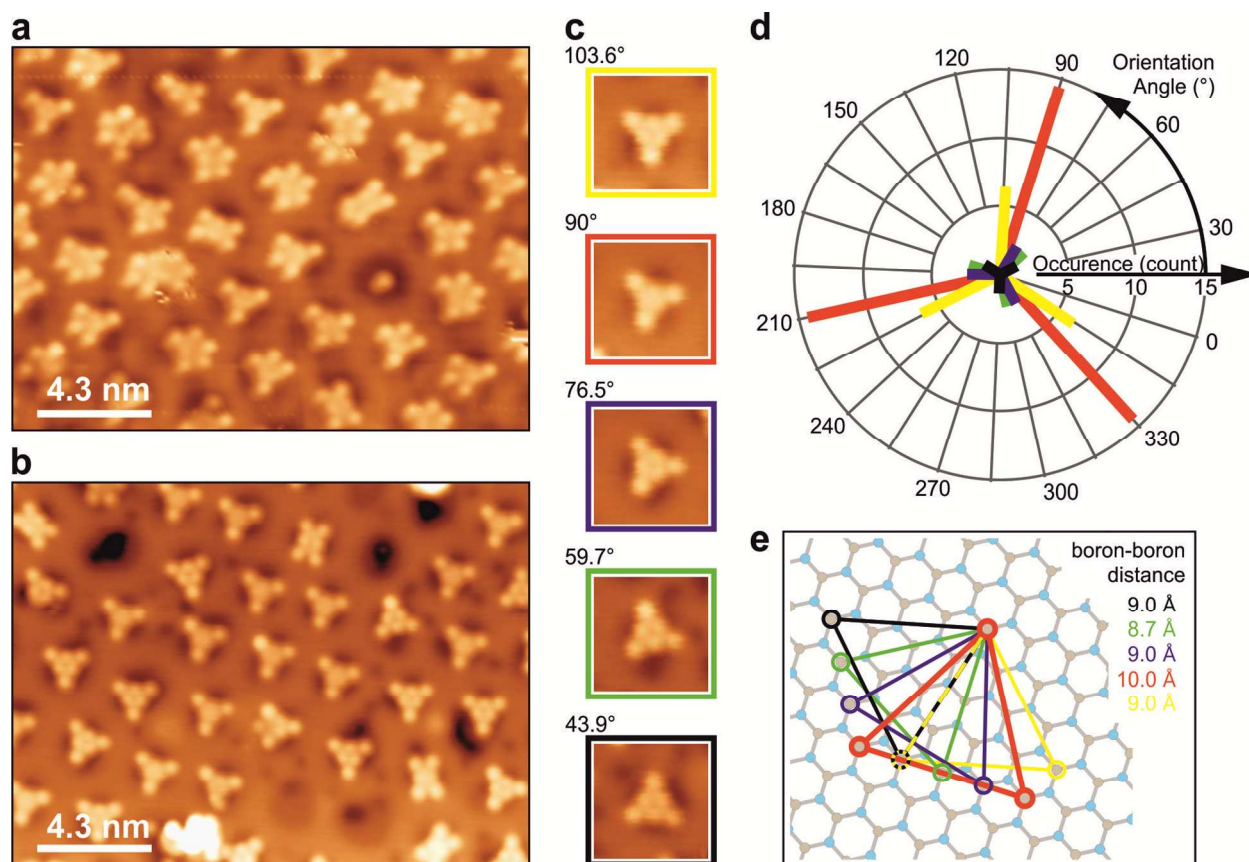
Figure 3: Iodine dissociation by thermal annealing. **a**, LT-STM image (1.2 V, 23 pA, height

scale: $\Delta z = 170$ pm) after annealing the sample to 500 K for 15 min. Either 1, 2, or 3 iodine

atoms have been dissociated per CHP molecule. Nearly all of the resulting species are oriented in

the same direction, independent of the number of dissociated iodine atoms. **b**, LT-STM image

(2 V, 40 pA, height scale: $\Delta z = 170$ pm) after treatment at 680 K for 30 min, leaving almost

exclusively I_3-CHP molecules. **c**, Zoomed view of selected species of (b) including angles of

rotation, showing differently pronounced protrusions close to the center of I_3-CHP molecules,

presumably due to the formation of carbon-boron bonds after iodine dissociation. **d**, Detailed

analysis of the orientations of dissociation sites in I_3-CHP in (b) relative to the corrugation lattice

of the *h*-BN on Rh(111) (colors refer to the specific orientations in c). The preferred orientation

is along the [12] direction (red bars). **e**, Geometric correlation between an undisturbed *h*-BN

lattice (lattice constant 2.5 Å) and the boron atoms presumably bonded to I_3-CHP (molecule

omitted for clarity). A smaller separation between these boron atoms corresponds to a stronger

tilt of the connected phenyl rings (triangles act as guides for the eye using the same colors as in

(c) and (d); red for regular dissociation in [12] direction).

The preference becomes less stringent under prolonged annealing conditions at higher

temperatures, where essentially I_3-CHP species are formed, but their rotational alignment within

the dents is no longer limited to the exclusive [12] direction (*cf.* LT-STM image after thermal

treatment at 680 K for 30 min. in Fig. 3b). This can be related to an increased mobility of the

molecules at elevated temperatures allowing the dissociation at previously inaccessible sites on

the *h*-BN lattice. Yet, the observable orientations of the I_3-CHP molecules are not random

(exemplary molecules and their occurrence are shown in Fig. 3c and d, respectively, with

predominant 90° orientation, *i.e.* alignment in the [12] direction) and the radical positions can be

tentatively related to the boron sites of the *h*-BN (Fig. 3e). In cases where the boron-boron

distance becomes smaller (all cases different from the [12] orientation) the protrusions are more

pronounced (*cf.* green and red in Fig. 3c), indicating a stronger tilt of the corresponding phenyl

rings. The significance of this circumstance will be discussed in the light of the DFT results.

Ab initio simulation of dehalogenation

To gain a deeper understanding of the unexpected site selectivity of the dehalogenation process

and its apparent persistence even at elevated temperatures, we need to answer the question,

which atomistic processes determine the peculiarity of the dehalogenation sites. So far we

showed that the registry between molecule and substrate yields two different configurations for

the iodine atoms (*A* and *B* sites) in alternating sequence on the I_6-CHP. While the DFT derived total dissociation energy for the first iodine atom from an I_6-CHP molecule on *h*-BN/Rh(111) exhibits only a small variation between *A* and *B*, the accompanying reorganization energies for the CHP remnant on the corrugated *h*-BN layer vary strongly with the actual iodine site. Evaluating the dissociation process shows that breaking the iodine-carbon bond is indeed accompanied by a bond formation between the unsaturated carbon atom of the iodine-free phenyl ring and the underlying boron atom of the *h*-BN. This bond instantly forms at *B* sites without moving the molecule (*cf.* Fig. 4c), while dissociation at an *A* site induces a displacement of the CHP remnant in order to let the unsaturated C atom approach the closest boron atom of the substrate and form the bond (Fig. 4a). This not only results in higher reorganization energies, *e.g.*, altered geometry of the dent, but also changes the registry between the CHP remnant and the substrate. Consequently, subsequent dehalogenation steps become less favorable. Figure 4e summarizes the DFT dissociation energies for some selected sequences, where the pure *B* site dissociations (*B-B-B* in Fig. 4e) form the energetically most favorable path of any triiodo-CHP final configuration.
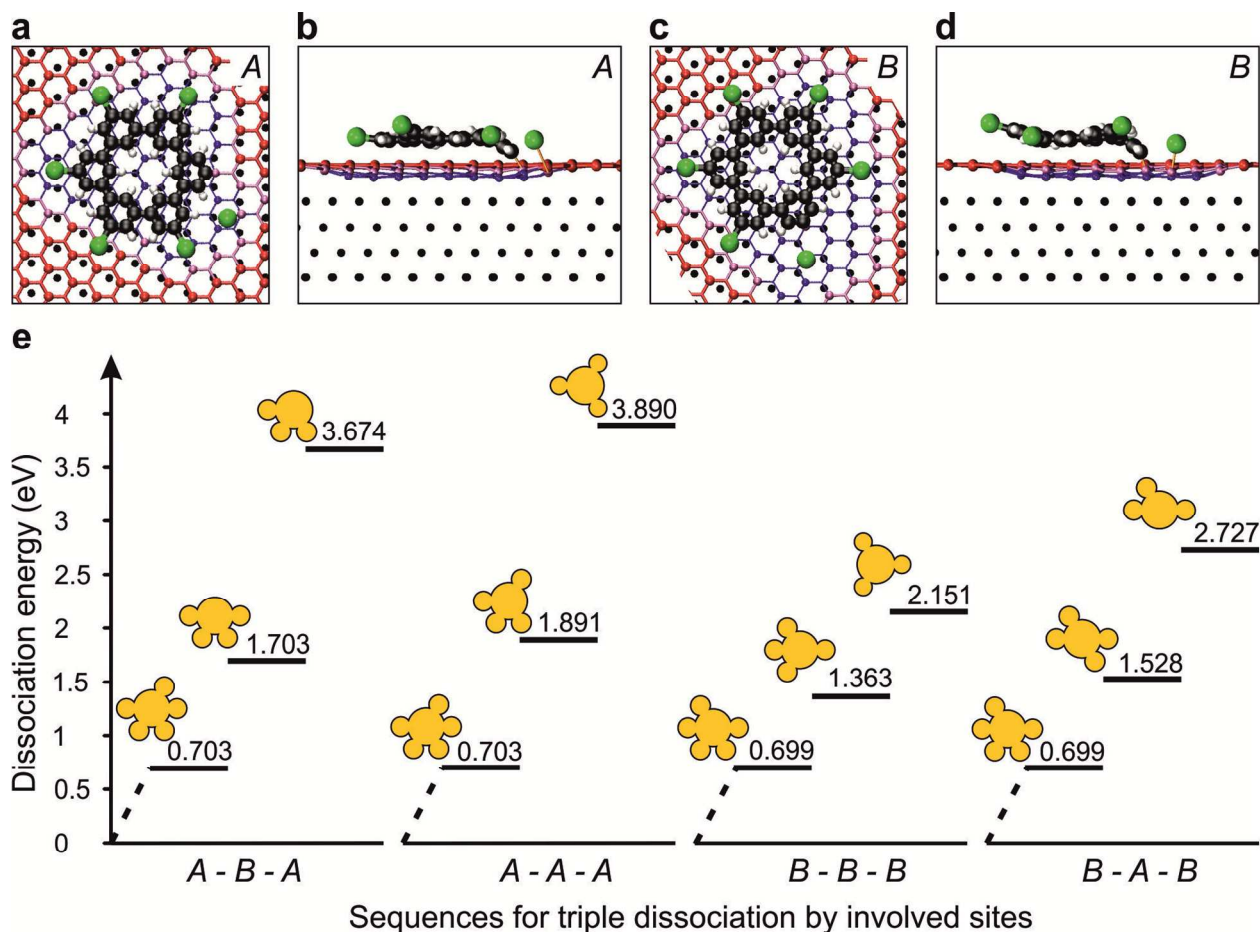
Figure 4: Dehalogenation by *ab initio* simulations. **a**, Dissociation at an *A* site resulting in a shift of the remaining molecule in the dent due to formation of a carbon-boron bond (CHP center no longer above nitrogen atom of *h*-BN). **b**, Side view indicating a strong tilt of the corresponding phenyl rings induced by the carbon-boron bond. **c**, After a dissociation at a *B* site, the molecule is still centered at the nitrogen atom, *i.e.*, no shift of the molecule within the dent. The side view shows a similar tilt of the corresponding phenyl ring (d). **e**, Dissociation energies (dissociated iodine atoms placed on wire) and illustrative pictograms of selected sequences representing the subsequent dehalogenation of I_6-CHP on *h*-BN, starting from a fully halogenated molecule. The energies given represent the sum of changes in total energy during subsequent dissociations necessary to create a certain I_3-CHP species.

The formation of a carbon-boron bond during dehalogenation slightly lifts the boron atom, still preserving the integrity of the *h*-BN lattice. The corresponding phenyl ring significantly tilts by 35° out of the molecular plane. This geometrical change explains the small protrusion appearing in the STM images close to the center of the CHP remnant towards the dehalogenated site (*cf.* Fig. 2). The lock-into-position of the molecule by the carbon-boron bond can only be overcome at elevated annealing temperatures, leading to molecule configurations with small-angle rotation to neighboring boron sites. These orientations of the molecule, which are off the [12] direction, are however not random but correspond again to well-defined geometrical positions of the carbon radical sites bonding to boron atoms of the *h*-BN (Fig. 3c). The difference in distance between the involved boron atoms (ranging from approx. 8.7 Å to 10 Å for the different rotational states) reveals itself in a varying accentuation of the STM-topographic substructure at the position of the cyclohexa-m-phenylene macrocycle. In other words, the registry with the underlying *h*-BN lattice defines the tilting angles of the phenyl rings as the molecular conformation must adapt itself to the shorter distance between the corresponding boron atoms (*cf.* Fig. 3c and e).

Oligomer formation by covalent coupling

So far, we have shown that for temperatures up to 680 K only approximately half of the iodine atoms are dissociated from I_6-CHP and the question arises whether controlled, direct aryl-aryl coupling between two dehalogenated molecules is possible. The barrier formed by the wire region between neighboring dents is conquerable by a higher surface coverage of I_6-CHP molecules, *i.e.*, decorating the wire regions of the *h*-BN corrugation. This raises the probability

that dehalogenated sites of neighboring molecules get in sufficiently close proximity of each other for the formation of dimers (*cf.* Fig. 5a). However, the annealing temperature of 550 K leaves a significant number of iodine atoms covalently bonded to the CHP core, some appearing significantly brighter in STM topography, because they are pushed onto the wire region of the corrugated *h*-BN as the restricted size of a dent cannot accommodate an entire dimer. The centers of the dimers exhibit a similar substructure of bright protrusions next to the dehalogenated sites as observed for monomers, due to tilted phenyl rings, indicating the presence of carbon-boron bonds (Fig. 5c). Reducing the number of bonded iodine atoms and facilitating the formation of extended oligomers requires annealing temperatures above 800 K. Consequently, a large variety of species and their orientation on the boron nitride can be observed.
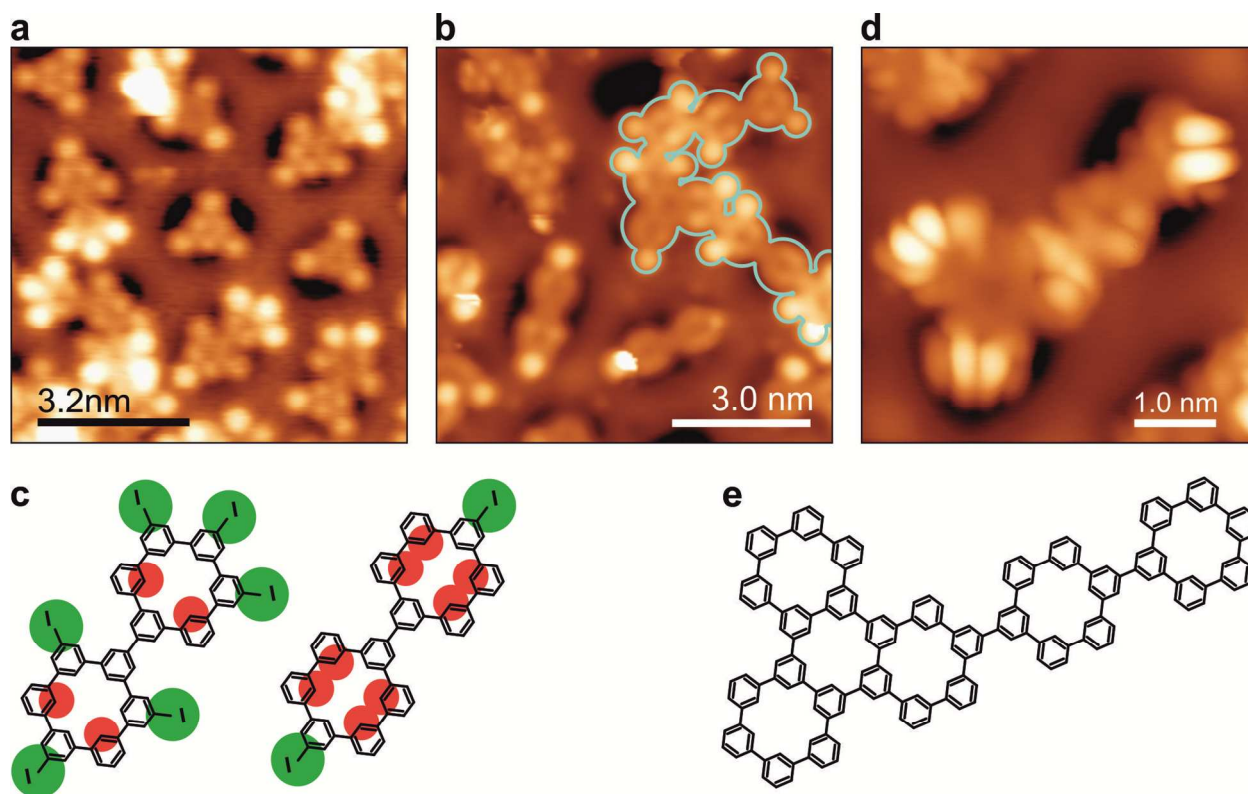
Figure 5: **Covalent coupling of CHP species at different temperatures. a,** STM image

(-1.5 V, 30 pA) of a high coverage sample (approx. 1 ML) after treatment at 550 K for 20 min.

Not only the expected I_3-CHP molecules have formed but various dimers with different iodine terminations are visible. **b,** STM image (-1.5 V, 30 pA) after treatment at 800 K for 30 min. Dimers and larger aggregates (light blue outline) have formed, but despite the high temperature still contain a notable number of iodine atoms. **c,** Illustrative sketch of two exemplary dimers observed in (a) and (b) (iodine atoms are shown in green, protrusion by tilted phenyl rings are highlighted in red). **d,** STM image (2.2 V, 20 pA) of a CHP oligomer coupled by high temperature treatment at 850 K for 30 min. The chain of coupled rings lies across two dents of the *h*-BN corrugation. **e,** Molecular structure of the CHP-based core of the oligomer shown in (d).

In Fig. 5b, almost iodine free dimers exist alongside extended oligomers. The outlined example is comprised of 9 CHP units and spans across several unit cells of the *h*-BN corrugation. The strong variation in appearance along the whole structure does not only originate from steric hindrance induced by the included iodine atoms, but also from bending across the wire region of the corrugation. Only at annealing temperatures of 850 K was it possible to produce iodine free oligomers as shown in Fig. 5d, where a chain of 5 connected CHP macrocycles can be seen (*cf.* Fig. 5e for structure of the CHP core). The fact that the structure bridges a wide area that exhibits strong variations of the surface potential[22] might contribute to the peculiar contrast in STM topography at the borders of the structure. The reason is that the locally varying surface potential can lead to an asymmetric shape of the frontier orbitals whose influence on the STM becomes important when scanning at high biases on insulating substrates.[32-34]

1
2
3
4
5
6
7
8
9
10
11
12
13
14
15
16
17
18
19
20
21
22
23
24
25
26
27
28
29
30
31
32
33
34
35
36
37
38
39
40
41
42
43
44
45
46
47
48
49
50
51
52
53
54
55
56
57
58
59
60

Conclusion

In-depth understanding of on-surface chemical reactions between molecular species and the underlying catalytic substrate with sub-molecular resolution is vital to the synthesis of active nanostructures for organic electronics. This is particularly the case for insulating substrates, which are technologically highly relevant but have not been widely investigated in this context. With the results presented here, we can directly correlate the adsorption position of the molecule and the possibility to produce the dehalogenated species necessary for the aryl-aryl coupling. The registry and unexpectedly strong interaction between the substrate and the molecules impose specific stable dehalogenated radical configurations. In the case of the I_6-CHP on the corrugated h-BN on Rh(111) this yields a large span in temperatures from the onset of dehalogenation at 500 K to full dehalogenation and coupling at 800 K. This is in strong contrast to metallic substrates like copper, silver or gold where full dehalogenation occurs already at room temperature, and also to the molecule in gas phase, where the dehalogenation sequence of the I_6-CHP is fully uncorrelated. In this respect it would be too simple to picture the effects of the h-BN only as an isotropic, reduced catalytic activity. We have shown that the interaction of the radical with the h-BN substrate is highly site specific and governs the dehalogenation sequence of the molecule. This poses a challenge for the controlled coupling. The imposed site selectivity could be of use for spatially precise dissociations towards dedicated reaction pathways. This, in turn, needs the precise matching between the molecule's sites of interest and the lattice constant of the h-BN. This substrate itself remains quite unaffected during the reactions and only provides the required bonding sites to stabilize the intermediate molecular species prior to subsequent reactions. Finally, the aryl-aryl coupling – similar to the metal mediated Ullmann coupling – was demonstrated on the insulating substrate. The understanding of these systems is another step

forward towards the design of electronic nanostructures on insulating or on other novel 2-dimensional substrates with reduced catalytic activity.

Methods

All experiments were performed in a UHV apparatus (base pressure $5*10^{-11}$ mbar) comprising a low-temperature scanning tunneling microscope operated at 5.5 K (LT-STM, Omicron). The rhodium single crystal (Rh(111)) is cleaned by repeated cycles of Ar^+ ion sputtering (750 eV, grazing incidence) and thermal annealing at 1200 K. Films of h-BN were grown by thermal dehydrogenation of borazine ($(HBNH)_3$, ~50 Langmuir) on the hot metal surface (1100 K)[23,26,29]. This is an almost self-limiting process, as the layer formation slows down once the first monolayer is completed. Subsequently, the sample is annealed at 1100 K for 15 min to promote uniform layer morphology. The preferential orientation of the *h*-BN on Rh(111) is deduced from energy dependent spot intensity analysis in Low Energy Electron Diffraction (LEED).[37] The D_{3h} symmetry given by the hcp- and fcc-hollow sites of the Rh(111) determines the orientation of the h-BN layer grown on it.[30] Afterwards, I_6-CHP molecules (see Ref. 38 for Synthesis) were deposited from a Knudsen cell, with a deposition rate of approx. 0.1 ML/min while keeping the substrate at room temperature. The Pt-Ir-tips were cut and optimised by slight indentation during usage. The software WSXM was used to analyse the STM images.[39]

The DFT calculations were performed using the CP2K package (CP2K version 2.3.43; CP2K is freely available in http://www.cp2k.org/) with the mixed Gaussian and plane wave formalism[40] and periodic boundary conditions. The exchange and correlation functional used was the revised[41] version of the Perdew-Burke-Ernzerhof (PBE)[42] function. Long-range dispersion interactions were included using the DFT-D3 formalism.[43] The core electrons were represented

by Goedecker-Teter-Hutter pseudopotentials.[44] Single- (for Rh), double- (B, N, C and I) and triple- (H and O) Zeta basis set including polarized function were employed to describe the valence electrons. The energy cutoff for the plane wave expansion representation was 500 Rydberg. The sampling in the Brillouin zone was made only at the Γ point. Due to the large size of the cell, such sampling is accurate. The size of the cell used in the calculations is 32.1195 Å in **a** and **b** directions and 25 Å along the surface normal **c**. This corresponds to a 12x12 four layers rhodium slab with a cell parameter of 3.785 Å and an adsorbed 13x13 h-BN monolayer. The dissociation energy is defined as the difference in total energy between the adsorbed, intact molecule and a configuration, where the dissociated iodine atoms are placed on the wire of the nanomesh.

ACKNOWLEDGMENT

ASSOCIATED CONTENT

Supporting Information Available: DFT results on the adsorption position and the dehalogenation in gas phase. Analysis of species created by thermal dehalogenation. This material is available free of charge *via* the Internet at http://pubs.acs.org.

REFERENCES

1   Novoselov, K. S.; Falko, V. I.; Colombo, L.; Gellert, P. R.; Schwab, M. G.; Kim, K. A.
     Roadmap for Graphene. *Nature* **2012**, *490*, 192–200.

2   Britnell, L.; Ribeiro, R. M.; Eckmann, A.; Jalil R.; Belle, B. D.; Mishchenko, A.; Kim, Y.-
     J.; Gorbachev, R. V.; Georgiou, T.; Morozov, S. V.; *et al.* Strong Light-Matter
     Interactions in Heterostructures of Atomically Thin Films. *Science* **2013**, *340*, 1311-1314.

3   Roth, S.; Matsui, F.; Greber, T.; Osterwalder, J.; Chemical Vapor Deposition and
     Characterization of Aligned and Incommensurate Graphene/Hexagonal Boron Nitride
     Heterostack on Cu(111). *NanoLett.* **2013**, *13*, 2668−2675.

4   Yang, W.; Chen, G.; Shi, Z.; Liu, C.-C.; Zhang, L.; Xie, G.; Cheng, M.; Wang, D.; Yang,
     R.; Shi, D.; *et al.* Epitaxial Growth of Single-Domain Graphene on Hexagonal Boron
     Nitride. *Nature Mater.* **2013**, *12*, 792–797.

5   Hunt, B.; Sanchez-Yamagishi, J.D.; Young, A.F.; Yankowitz, M.; LeRoy, B.J.; Watanabe,
     K.; Taniguchi, T.; Moon, P.; Koshino, M.; Jarillo-Herrero, P.; *et al.* Massive Dirac
     Fermions and Hofstadter Butterfly in a van der Waals Heterostructure. *Science* **2013**, *340*,
     1427-1430.

6   Méndez, J.; López, M. F.; Martin-Gago, J.; On-Surface Synthesis of Cyclic Organic
     Molecules. *Chem. Soc. Rev.* **2011**, *40*, 4578-4590.

7   Ertl, G.; Freund, H. J. Catalysis and Surface Science. *Phys. Today* **1999**, *52*, 32.

8   Somorjai, G. A. Surface Science and Catalysis. *Science* **1985**, 227, 902-908.

9   Grill, L.; Dyer, M.; Lafferentz, L.; Persson, M.; Peters, M.V.; Hecht, S. Nano-

Architectures by Covalent Assembly of Molecular Building Blocks. *Nat. Nanotechnol.* **2007**, *2*, 687–691.

10   Ullmann, F.; Bielecki, J. Ueber Synthesen in der Biphenylreihe. *Ber. Dtsch. Chem. Gesell.* **1901**, *34*, 2174–2185.

11   Ullmann, F. Ueber symmetrische Biphenylderivate. *Liebigs Ann. Chem.* **1904**, *332*, 38–81.

12   Hla, S.-W.; Bartels, L.; Meyer, G.; Rieder, K.-H. Inducing All Steps of a Chemical Reaction with the Scanning Tunneling Microscope Tip: Towards Single Molecule Engineering. *Phys. Rev. Lett.* **2000**. *85*, 2777.

13   Cai, J.; Ruffieux, P.; Jaafar, R.; Bieri, M.; Braun, T.; Blankenburg, S.; Muoth, M.; Seitsonen, A.P.; Saleh, M.; Feng, X.; *et al.* Atomically Precise Bottom-Up Fabrication of Graphene Nanoribbons. *Nature* **2010**, *466*, 470–473.

14   Bieri, M.; Treier, M.; Cai, J.; Aït-Mansour, K.; Ruffieux, P.; Gröning, O.; Gröning, P.; Kastler, M.; Rieger, R.; Feng, X.; *et al.* Porous Graphenes: Two-Dimensional Polymer Synthesis with Atomic Precision. *Chem. Comm.* **2009**, *45*, 6919–6921.

15   Bieri, M.; Nguyen, M.-T.; Gröning, O.; Cai, J.; Treier, M.; Aït-Mansour, K.; Ruffieux, P.; Pignedoli, C.A.; Passerone, D.; Kastler, M.; *et al.* Two-Dimensional Polymer Formation on Surfaces: Insight into the Roles of Precursor Mobility and Reactivity. *J. Amer. Chem. Soc.* **2010**, *132*, 16669–16676.

16   Sachdev, H.; Mueller, F.; Huefner, S. BN Analogues of Graphene: On the Formation Mechanism of Boronitrene Layers - Solids with Extreme Structural Anisotropy. *Diam. Relat. Mater.* **2010**, *19*, 1027-1033.

17   Auwärter, W.; Muntwiler, M.; Osterwalder, J.; Greber, T. Defect Lines and Two-Domain Structure of Hexagonal Boron Nitride Films on Ni(111). *Surf. Sci. Lett.* **2003**, *545*, L735–L740.

18   Preobrajenski, A. B.; Vinogradov, A. S.; Ng, M.L.; Ćavar, E.; Westerström, R.; Mikkelsen, A.; Lundgren, E.; Mårtensson, N. Influence of Chemical Interaction at the Lattice-mismatched h-BN/Rh(111) and h-BN/Pt(111) Interfaces on the Overlayer Morphology. *Phys. Rev. B* **2007**, *75*, 245412.

19   Joshi, S.; Ecija, D.; Koitz, R.; Iannuzzi, M.; Seitsonen, A.P.; Hutter, J.; Sachdev, H.; Vijayaraghavan S.; Bischoff, F.; Seufert, K.; *et al.* Boron Nitride on Cu(111): An Electronically Corrugated Monolayer. *Nano Lett.* **2012**, *12*, 5821–5828.

20   Corso, M.; Auwärter, W.; Muntwiler, M.; Tamai, A.; Greber, T.; Osterwalder, J. Boron Nitride Nanomesh. *Science* **2004**, *303*, 217-220.

21   Bunk, O.; Corso, M.; Martoccia, D.; Herger, R.; Willmott, P.R.; Patterson, B.D.; Osterwalder, J.; van der Veen, J.F.; Greber, T. Surface X-ray Diffraction Study of Boron-Nitride Nanomesh in Air. *Surf. Sci.* **2007**, *601*, L7-L10.

22   Dil, H.; Lobo-Checa, J.; Laskowski, R.; Blaha, P.; Berner, S.; Osterwalder, J.; Greber, T. Surface Trapping of Atoms and Molecules with Dipole Rings, *Science* **2008**, *319*, 1824.

23   Berner, S.; Corso, M.; Widmer, R.; Groening, O.; Laskowski, R.; Blaha, P.; Schwarz, K.; Goriachko, A.; Over, H.; Gsell, S.; *et al.* Boron Nitride Nanomesh: Functionality from a Corrugated Monolayer. *Angew. Chem. Int. Ed.* **2007**, *46*, 5115 –5119.

24   Martoccia, D.; Pauli, S.A.; Brugger, T.; Greber, T.; Patterson, B.D.; Willmott, P.R. h-BN

on Rh(111): Persistence of a Commensurate 13-on-12 Superstructure up to High Temperatures. *Surf. Sci.* **2010**, *604*, L9–L11.

25   Martoccia, D.; Brugger, T.; Björck, M.; Schlepütz, C.M.; Pauli, S.A.; Greber, T.; Patterson, B.D.; Willmott, B.D. H-BN/Ru(0001) Nanomesh: A 14-on-13 Superstructure with 3.5 nm Periodicity. *Surf. Sci.* **2010**, *604*, L16–L19.

26   Widmer, R.; Passerone, D.; Mattle, T.; Sachdev, H.; Gröning, O. Probing the Selectivity of a Nanostructured Surface by Xenon Adsorption. *Nanoscale* **2010**, *2*, 502.

27   Vinogradov, N. A.; Zakharov, A. A.; Ng, M.L.; Mikkelsen, A.; Lundgren, E.; Mårtensson, N.; Preobrajenski, A.B. One-Dimensional Corrugation of the h-BN Monolayer on Fe(110). *Langmuir* **2012**, *28*, 1775−1781.

28   Müller, F.; Hüfner, S.; Sachdev, H. One-Dimensional Structure of Boron Nitride on Chromium (110) – a Study of the Growth of Boron Nitride by Chemical Vapour Deposition of Borazine. *Surf. Sci.* **2008**, *602*, 3467–3476.

29   Müller, F.; Hüfner, S.; Sachdev, H. Epitaxial Growth of Boron Nitride on a Rh(111) Multilayer System: Formation and Fine Tuning of a BN-Nanomesh. *Surf. Sci.* **2009**, *603*, 425–432.

30   Laskowski, R.; Blaha, P.; Gallauner, T.; Schwarz, K. Single-Layer Model of the Hexagonal Boron Nitride Nanomesh on the Rh(111) Surface. *Phys. Rev. Lett.* **2007**, 98, 106802.

31   Gomez Diaz, J.; Ding, Y.; Koitz, R.; Seitsonen, A.P.; Iannuzzi M.; Hutter, J. Hexagonal Boron Nitride on Transition Metal Surfaces. *Theor. Chem. Acc.* **2013**, *132*, 1350.

32   Repp, J.; Meyer, G.; Olsson, F. E.; Persson, M. Controlling the Charge State of Individual Gold Adatoms. *Science* **2004**, 305, 493-495.

33   Repp, J.; Meyer, G.; Paavilainen, S.; Olsson, F. E.; Persson, M. Imaging Bond Formation Between a Gold Atom and Pentacene on an Insulating Surface. *Science* **2006**, *312*, 1196-1199.

34   Repp, J.; Meyer, G. Scanning Tunneling Microscopy of Adsorbates on Insulating Films. From the Imaging of Individual Molecular Orbitals to the Manipulation of the Charge State. *Appl. Phys. A* **2006**, *85*, 399-406.

35   Kunstmann, T.; Schlarb, A.; Fendrich, M.; Wagner, T.; Möller R.; Hoffmann, R.; Dynamic Force Microscopy Study of 3,4,9,10-Perylenetetracarboxylic Dianhydride on KBr(001). *Phys. Rev. B* **2005**, *71*, 121403(R).

36   Dienel, T.; Loppacher, C.; Mannsfeld, S. C. B.; Forker, R.; Fritz, T. Growth-Mode-Induced Narrowing of Optical Spectra of an Organic Adlayer. *Adv. Mater.* **2008**, *20*, 959–963.

37   Van Hove, M. A.; Koestner, R. J. in Determination of Surface Structure by LEED; Marcus, P. M., Jona, F., Eds.; Plenum Press: New York and London, 1984, p. 357.

38   Horcas, I.; Fernández, R.; Gómez-Rodríguez, J.M.; Colchero, J.; Gómez-Herrero, J.; Baro, A.M. WSXM: A Software for Scanning Probe Microscopy and a Tool for Nanotechnology. *Rev. Sci. Instrum.* **2007**, *78*, 013705.

39   Pisula, W.; Kastler, M.; Yang, C.; Enkelmann, V.; Mullen, K. Columnar Mesophase Formation of Cyclohexa-m-phenylene-Based Macrocycles. *Chem. Asian J.* **2007**, *2*, 51-

56.

40   Lippert, G.; Hutter, J.; Parrinello, M. A hybrid Gaussian and Plane Wave Density

      Functional Scheme. *Mol. Phys.* **1997**, *92*, 477-487.

41   Zhang, Y.; Yang, W. Comment on "Generalized Gradient Approximation Made Simple

      [Perdew, J.P.; Burke, K.; Ernzerhof, M. Phys. Rev. Lett. 77, 3865–3868 (1996)]". *Phys.*

      Rev. Lett. **1998**, *80*, 890–891.

42   Perdew, J. P.; Burke, K.; Ernzerhof, M. Generalized Gradient Approximation Made

      Simple. *Phys. Rev. Lett.* **1996**, *77*, 3865-3868.

43   Grimme, S.; Antony, J.; Ehrlich, S.; Krieg, H. A Consistent and Accurate Ab Initio

      Parametrization of Density Functional Dispersion Correction (DFT-D) for the 94

      Elements H-Pu. *J. Chem. Phys.* **2010**, *132*, 154104.

44   Goedecker, S.; Teter, M.; Hutter, J. Separable Dual-Space Gaussian Pseudopotentials.

      Phys. Rev. B **1996**, *54*, 1703-1710.

AUTHOR INFORMATION

Corresponding Author

* Thomas Dienel: thomas.dienel@empa.ch; * Oliver Gröning: oliver.groening@empa.ch

Swiss Federal Laboratories for Materials Science and Technology

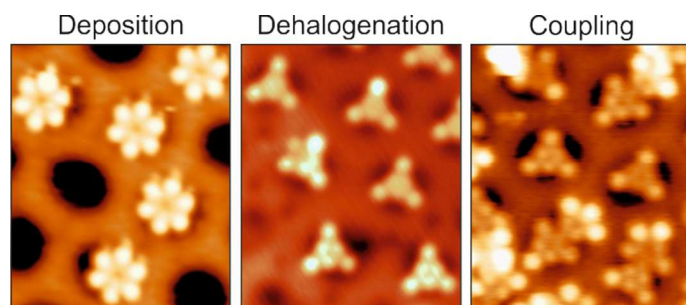nanotech@surfaces Laboratory

Ueberlandstrasse 129

CH-8600 Duebendorf

Switzerland

Author Contributions

T.D. and K.R. performed the STM measurements. T.D., R.W., and O.G. analyzed the data and

discussed the results. J.G.-D., A.P.S., M.I., and J.H. performed the DFT calculations. H.S. and

K.M. provided the molecules. T.D. and A.P.S. wrote the manuscript with inputs from all other

authors.

Notes

† Jaime Gómez-Díaz: Deceased.

TOC FIGURE

| Deposition | Dehalogenation | Coupling |